Article:
(2024) Measurement of the Yb 176 (n,γ) cross section at the n_TOF facility at CERN. Physical Review C. 064619. ISSN 2469-9993

https://doi.org/10.1103/PhysRevC.110.064619

Measurement of the ^{176}Yb(n, γ) cross section at the n_TOF facility at CERN

F. García-Infantes,[1,2] J. Praena,[1,2] A. Casanovas-Hoste,[3] R. Henkelmann,[4] U. Köster,[5] O. Aberle,[2] V. Alcayne,[6] S. Altieri,[7,8] S. Amaducci,[9] H. Amar Es-Sghir,[1] J. Andrzejewski,[10] V. Babiano-Suarez,[3] M. Bacak,[2] J. Balibrea-Correa,[3] S. Bennett,[11] A. P. Bernardes,[2] E. Berthoumieux,[12] D. Bosnar,[13] M. Busso,[14,15] M. Caamaño,[16] F. Calviño,[17] M. Calviani,[2] D. Cano-Ott,[6] D. M. Castelluccio,[18,19] F. Cerutti,[2] G. Cescutti,[20,21] S. Chasapoglou,[22] E. Chiaveri,[2,11] P. Colombetti,[23,24] N. Colonna,[25] P. Console Camprini,[18,19] G. Cortés,[17] M. A. Cortés-Giraldo,[26] L. Cosentino,[9] S. Cristallo,[14,27] M. Di Castro,[2] D. Diacono,[25] M. Diakaki,[22] M. Dietz,[28] C. Domingo-Pardo,[3] R. Dressler,[29] E. Dupont,[12] I. Durán,[16] Z. Eleme,[30] S. Fargier,[2] B. Fernández-Domínguez,[16] P. Finocchiaro,[9] S. Fiore,[18,31] V. Furman,[32] A. Gawlik-Ramięga,[10] G. Gervino,[23,24] S. Gilardoni,[2] E. González-Romero,[6] C. Guerrero,[26] F. Gunsing,[12] C. Gustavino,[31] J. Heyse,[33] D. G. Jenkins,[34] E. Jericha,[35] A. Junghans,[36] Y. Kadi,[2] T. Katabuchi,[37] I. Knapová,[38] M. Kokkoris,[22] Y. Kopatch,[32] M. Krtička,[38] D. Kurtulgil,[39] I. Ladarescu,[3] C. Lederer-Woods,[40] J. Lerendegui-Marco,[3] G. Lerner,[2] A. Manna,[19,41] T. Martínez,[6] M. Martínez-Cañada,[1] A. Masi,[2] C. Massimi,[19,41] P. Mastinu,[42] M. Mastromarco,[25,43] F. Matteucci,[20,21] E. A. Maugeri,[29] A. Mazzone,[25,44] E. Mendoza,[6] A. Mengoni,[18,19] V. Michalopoulou,[22,2] P. M. Milazzo,[20] R. Mucciola,[14,15] F. Murtas,[45] E. Musacchio González,[42] A. Musumarra,[46,47] A. Negret,[48] A. Oprea,[48] P. Pérez-Maroto,[26] N. Patronis,[30] J. A. Pavón-Rodríguez,[26,2] M. G. Pellegriti,[46] J. Perkowski,[10] C. Petrone,[48] L. Piersanti,[14,27] E. Pirovano,[28] S. Pomp,[49] I. Porras,[1] N. Protti,[7,8] J. M. Quesada,[26] T. Rauscher,[50,51] R. Reifarth,[39] D. Rochman,[29] Y. Romanets,[52] F. Romano,[46] C. Rubbia,[2] A. Sánchez-Caballero,[6] M. Sabaté-Gilarte,[2] P. Schillebeeckx,[33] D. Schumann,[29] A. Sekhar,[11] A. G. Smith,[11] N. V. Sosnin,[40] M. Spelta,[19,41] M. E. Stamati,[30,2] G. Tagliente,[25] A. Tarifeño-Saldivia,[17] D. Tarrío,[49] N. Terranova,[18,45] P. Torres-Sánchez,[1] S. Urlass,[36,2] S. Valenta,[38] V. Variale,[25] P. Vaz,[52] D. Vescovi,[39] V. Vlachoudis,[2] R. Vlastou,[22] A. Wallner,[53] P. J. Woods,[40] T. Wright,[11] and P. Žugec[13]

(n_TOF Collaboration)

[1]*University of Granada, Spain*

[2]*European Organization for Nuclear Research (CERN), Switzerland*

[3]*Instituto de Física Corpuscular, CSIC–Universidad de Valencia, Spain*

[4]*Isotope Technology Munich (ITM), Germany*

[5]*Institut Laue-Langevin (ILL), Grenoble, France*

[6]*Centro de Investigaciones Energéticas Medioambientales y Tecnológicas (CIEMAT), Spain*

[7]*Istituto Nazionale di Fisica Nucleare, Sezione di Pavia, Italy*

[8]*Department of Physics, University of Pavia, Italy*

[9]*INFN Laboratori Nazionali del Sud, Catania, Italy*

[10]*University of Lodz, Poland*

[11]*University of Manchester, United Kingdom*

[12]*CEA Irfu, Université Paris-Saclay, F-91191 Gif-sur-Yvette, France*

[13]*Department of Physics, Faculty of Science, University of Zagreb, Zagreb, Croatia*

[14]*Istituto Nazionale di Fisica Nucleare, Sezione di Perugia, Italy*

[15]*Dipartimento di Fisica e Geologia, Università di Perugia, Italy*

[16]*University of Santiago de Compostela, Spain*

[17]*Universitat Politècnica de Catalunya, Spain*

[18]*Agenzia nazionale per le nuove tecnologie, l'energia e lo sviluppo economico sostenibile (ENEA), Italy*

[19]*Istituto Nazionale di Fisica Nucleare, Sezione di Bologna, Italy*

[20]*Istituto Nazionale di Fisica Nucleare, Sezione di Trieste, Italy*

[21]*Department of Physics, University of Trieste, Italy*

[22]*National Technical University of Athens, Greece*

[23]*Istituto Nazionale di Fisica Nucleare, Sezione di Torino, Italy*

[24]*Department of Physics, University of Torino, Italy*

[25]*Istituto Nazionale di Fisica Nucleare, Sezione di Bari, Italy*

[26]*Universidad de Sevilla, Spain*

[27]*Istituto Nazionale di Astrofisica–Osservatorio Astronomico d'Abruzzo, Italy*

[28]*Physikalisch-Technische Bundesanstalt (PTB), Bundesallee 100, 38116 Braunschweig, Germany*

[29]*Paul Scherrer Institut (PSI), Villigen, Switzerland*
[30]*University of Ioannina, Greece*
[31]*Istituto Nazionale di Fisica Nucleare, Sezione di Roma1, Roma, Italy*
[32]*Affiliated with an institute covered by a cooperation agreement with CERN*
[33]*European Commission, Joint Research Centre (JRC), Geel, Belgium*
[34]*University of York, United Kingdom*
[35]*TU Wien, Atominstitut, Stadionallee 2, 1020 Wien, Austria*
[36]*Helmholtz-Zentrum Dresden-Rossendorf, Germany*
[37]*Tokyo Institute of Technology, Japan*
[38]*Charles University, Prague, Czech Republic*
[39]*Goethe University Frankfurt, Germany*
[40]*School of Physics and Astronomy, University of Edinburgh, United Kingdom*
[41]*Dipartimento di Fisica e Astronomia, Università di Bologna, Italy*
[42]*INFN Laboratori Nazionali di Legnaro, Italy*
[43]*Dipartimento Interateneo di Fisica, Università degli Studi di Bari, Italy*
[44]*Consiglio Nazionale delle Ricerche, Bari, Italy*
[45]*INFN Laboratori Nazionali di Frascati, Italy*
[46]*Istituto Nazionale di Fisica Nucleare, Sezione di Catania, Italy*
[47]*Department of Physics and Astronomy, University of Catania, Italy*
[48]*Horia Hulubei National Institute of Physics and Nuclear Engineering, Romania*
[49]*Department of Physics and Astronomy, Uppsala University, Box 516, 75120 Uppsala, Sweden*
[50]*Department of Physics, University of Basel, Switzerland*
[51]*Centre for Astrophysics Research, University of Hertfordshire, Hatfield AL10 9AB, United Kingdom*
[52]*Instituto Superior Técnico, Lisbon, Portugal*
[53]*Australian National University, Canberra, Australia*

(Received 30 July 2024; accepted 8 November 2024; published 27 December 2024)

Background: The ^{176}Yb$(n,\gamma)^{177}$Yb $\rightarrow$ ^{177}Lu reaction is of interest in nuclear medicine as it is the preferred production route for ^{177}Lu. This radioisotope has seen a very fast growth of usage in nuclear medicine in recent years due to its outstanding properties. New data on this reaction could provide useful information for production at new facilities.
Purpose: We aim to resolve resonances in the ^{176}Yb$(n,\gamma)^{177}$Yb reaction for the first time. Previous capture measurement provided data at thermal point and encompassed integral measurements in the range from 3 keV to 1 MeV, where three time-of-flight measurements are available, but with low resolution to resolve the resonances. Transmission measurements from the 1970s resolved and analyzed some resonances.
Method: We measure the neutron capture cross section of ^{176}Yb$(n,\gamma)^{177}$Yb by means of the time-of-flight technique at the Experimental Area 1 of the n_TOF facility at CERN using an enriched $^{176}Yb_2O_3$ sample and an array of four C_6D_6 liquid scintillation detectors.
Results: We have resolved 164 resonances up to 21 keV, including 96 new ones. We also provide new capture experimental data from 90 eV to 3 keV, and we extend the resolved resonance region up to 21 keV. In addition, resonance decay widths, Γ_γ and Γ_n, are provided for all resonances together with resonance energies.
Conclusions: The ^{176}Yb$(n,\gamma)^{177}$Yb reaction has been measured, providing resonance parameters for the first time from a few eV to 21 keV. The analysis of the resonances has been carried out and compared with previous works and existing libraries, revealing discrepancies due to the new information on Γ_γ parameters. Our results are consistent with the Γ_n parameters obtained in transmission measurements.

DOI: 10.1103/PhysRevC.110.064619

I. INTRODUCTION

The lanthanides, a group of 15 metallic elements from lanthanum (La) to lutetium (Lu), are increasingly recognized for their pivotal roles in various advanced technological applications. For instance, lanthanides are integral components in a variety of devices due to the magnetic, optical, and catalytic properties of these elements. They are further essential part of the production of high-performance magnets, phosphors in light-emitting diodes (LEDs), and various catalytic converters [1].

In nuclear astrophysics, the lanthanides are of particular importance to study the nucleosynthesis of the heavy elements since their solar abundances are much better defined than those of other elements [2]. The contribution of the slow neutron capture process (*s* process) to the lanthanides takes place during He shell burning in low mass AGB stars [2].

They are also expected to be produced during the rapid process (r process). Neutron capture cross sections of ytterbium isotopes have been studied providing key information for both processes. Accordingly, ^{170}Yb is s-only isotope, therefore, it provides a direct measure for the weak branchings in this mass region [2]. Meanwhile, ^{176}Yb is a r-process dominated isotope [3], which may provide information on magnetorotational-driven supernovae, collapsars and neutron-star mergers [4].

In addition, the unique electronic configurations of lanthanides make them essential in medical nuclear imaging and therapy. Indeed, ^{177}Lu is the radioisotope with a very fast growth of usage in nuclear medicine in recent years due to the possibility to be incorporated to different molecules as ^{177}Lu-DOTATATE [5], ^{177}Lu-PSMA [6], and many others under development. ^{177}Lu decays with a half-life of $T_{1/2} = 6.643(11)$ days to stable ^{177}Hf by emitting low-energy βs, accompanied by γ rays of 113 and 208 keV useful for imaging purposes [7]. At present, two routes are employed for the production of ^{177}Lu in nuclear reactors: the direct or carrier-added (ca) route, ^{176}Lu$(n,\gamma)^{177,177m}$Lu and the indirect or non-carrier-added (nca) route, ^{176}Yb$(n,\gamma)^{177}$Yb ($t_{1/2} \approx 1.9$ h) $\rightarrow$ ^{177}Lu. Currently, the use of nca is preferred because it avoids coproduction of long-lived ^{177m}Lu that can cause waste handling issues in hospitals [8,9].

The ^{176}Yb$(n,\gamma)^{177}$Yb reaction has a relatively low thermal cross-section of 2.85(5) b [10], i.e., neutron self-attenuation in the irradiation targets is not very pronounced and ^{176}Yb targets can be scaled to large sizes. Supplementary ^{177}Yb production occurs by epithermal neutron capture with a resonance integral of 6.9(6) b, but this energy regime is characterized by individual resonances with much higher cross-sections. Hence, neutron self-attenuation in extended ^{176}Yb targets is more pronounced for the most useful neutron energies (at the resonances). A detailed knowledge of the resonance parameters is required to simulate production by epithermal neutron capture and optimize this contribution for different target characteristics and geometries.

The available experimental data for the ^{176}Yb$(n,\gamma)^{177}$Yb reaction have primarily focused on thermal energies [11–14] and above 3 keV [2,15–18]. Furthermore, the absence of resolved resonances for the capture reaction is apparent, even though resonances have been successfully identified in transmission experiments [19,20]. Regarding evaluations, ENDF/B-VIII.0 [21], TENDL-2021 [22], and JEFF-3.3 [23] report (individual) resonance information up to 5, 20, and 26 keV, respectively. These libraries agree on the number of resonances up to 5 keV, with some discrepancies in the resonance parameters between JEFF-3.3 and the other two. However, beyond 5 keV, notable discrepancies emerge. The goal of the present work is the measurement and analysis of the resonances of the ^{176}Yb$(n,\gamma)^{177}$Yb reaction for the first time.

II. MEASUREMENT AT n_TOF

A. n_TOF facility at CERN

The Neutron Time-of-Flight facility, n_TOF [24], is a spallation neutron source located at CERN [25]. The neutrons are produced by spallation reactions induced by 20 GeV/c proton pulses extracted from the proton synchrotron (PS) and directed toward a lead target. These pulses, with a nominal intensity of 8.5×10^{12} protons, *are delivered with a time width of each pulse of 7 ns root-mean-squared (RMS)* [26,27].

The (outgoing) high-energy (MeV to GeV) neutrons are then moderated by a layer of water surrounding the target to achieve a white energy spectrum spanning from GeV down to thermal energies. The neutrons travel toward the two experimental areas along two beam lines: EAR1, located 185 m away from the spallation target, is primarily utilized for high neutron energy resolution measurements [26]. Conversely, EAR2, located at the end of a 19 m vertical beam line, makes it especially appropriate for measurements of low mass and/or radioactive samples thanks to its high instantaneous neutron flux, 30 times greater than EAR1, and currently the highest in the world [28–30]. In addition, a new experimental area, the NEAR station, located ∼3 m from the target, was commissioned in 2021 [31]. The measurement of the ^{176}Yb(n,γ) reaction, aimed at providing more complete and accurate information in the resolved resonance region (RRR), was therefore carried out at EAR1.

B. Samples and ancillary measurements

The measurement campaign was conducted using 1.5976(1) g of $^{176}Yb_2O_3$ in powder form, enriched to 99.43% in ^{176}Yb. The exact isotopic composition is given in Table I. The oxide powder was encapsulated in a high-purity quartz cuvette having external dimensions of 22 mm in diameter and 4.5 mm in thickness. The inner part of the cuvette had dimensions of 19 mm in diameter and 2 mm in thickness, representing the dimensions of our sample. The entrance point of the cuvette was closed with a polyethylene cap, and once it was filled with the $^{176}Yb_2O_3$ powder, it was sealed by a glassblower before being delivered for the experiment. The sample was produced and provided by Henkelmann from ITM Radiopharma GmbH. The quartz cuvette, both with and without Yb, is depicted in Fig. 1.

A total of $1.74 \cdot 10^{18}$ protons—equivalent to 16 days of beam time—were utilized during the experimental campaign, with 58% dedicated to the ^{176}Yb sample. Ancillary measurements are essential for an accurate analysis of the capture data. The background generated by the quartz container was evaluated by measuring an identical empty capsule, hereafter referred to as "dummy." Additional beam time was dedicated to measure carbon and lead samples to estimate the background due to scattering of neutrons and in-beam γ rays in the Yb sample. Absolute yield normalization was achieved via the saturated resonance method [32], which required measuring a thick (50 μm) gold sample with the same diameter as the sample. Additionally, measurements without a target in the beam

TABLE I. Isotopic composition of the ^{176}Yb sample.

Isotope	^{168}Yb	^{170}Yb	^{171}Yb	^{172}Yb	^{173}Yb	^{174}Yb	^{176}Yb
Perc. (%)	0.006	0.015	0.083	0.018	0.119	0.329	99.43

FIG. 1. Left: The sealed cuvette with $^{176}Yb_2O_3$ powder. Right: An empty quartz cuvette with its polyethylene cap.

were necessary to estimate background levels in the carbon, lead, and gold measurements. Details about the background subtraction are provided in Sec. III E.

C. Experimental setup

To determine experimentally the capture cross section, two primary techniques are employed at n_TOF: the total absorption technique, which involves detecting the complete γ-ray cascade using a 4π BaF_2 total absorption calorimeter [33], and the total energy detection technique (TED) [34], which consists of detecting at most one γ ray from each cascade using an array of low neutron sensitivity scintillation detectors. To avoid the dependency of the detection efficiency on the energy of the registered γ ray, the TED technique requires the use of the pulse height weighting technique (PWHT) [35], a procedure that will be explained in more detail in Sec. III A.

The present measurement was conducted using the setup depicted in Fig. 2. It consisted of an array of four liquid organic scintillation detectors, each of them with one liter of highly purified deuterated benzene (C_6D_6) as active material. These detectors are characterized by having very fast rise and narrow signal width times, in addition to exhibiting a rapid recovery after signal detection of the prompt γ rays produced in the spallation reactions (also referred to as "γ-flash"), making them particularly suitable for time-of-flight (TOF) measurements. The detectors were positioned facing the sample at distance of 10 cm and at an angle of 125° with respect to the beam direction. This orientation was chosen to minimize the impact of possible anisotropies in the emission of capture γ rays [36], as well as to reduce the background generated by the in-beam γ rays scattered by the sample.

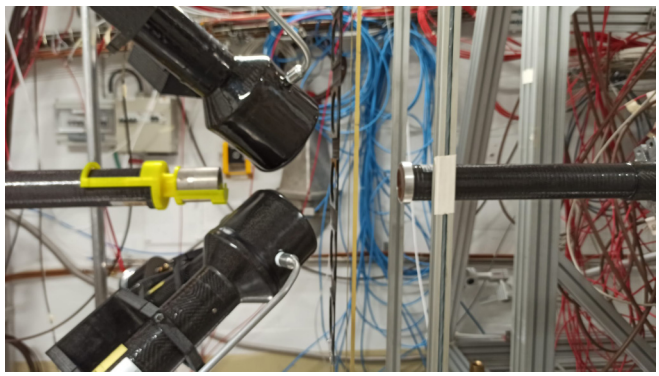

FIG. 2. General view of the experimental setup at EAR1 used for the $^{176}Yb(n,\gamma)$ measurement. Four C_6D_6 detectors are set up surrounding the capture sample.

To monitor the beam, three additional detectors were employed to oversee both the proton and neutron beams. The monitors for the proton beam include the beam current transformer [24] and the wall current monitor [37], positioned in the vacuum pipe connecting the PS accelerator and the spallation target. These devices measure the intensity of the proton beam in each pulse. The neutron beam is directly monitored by the Silicon Monitor detector [38]. The monitoring principle is based on the neutron-converting reaction $^6Li(n,\alpha)\,^3H$.

Each detector in the capture setup and beam monitoring system is connected to a channel of the n_TOF data acquisition system, which utilizes SPDevices ADQ14DC flash analog-to-digital units. These units offer four channels with 14-bit resolution, a sample rate of up to 1 GS/s, a buffer memory of 256 MS, and a bandwidth of 400 MHz [39,40]. The raw data from all detectors for multiple proton bunches or "events" are temporarily stored in a local computer file, automatically transferred to the CERN tape archive [41] for their long-term storage and subsequent off-line analysis, replacing the previous CERN Advanced STORage manager [42].

III. ANALYSIS

The detection efficiency typically depends on the cascade pattern, such as the γ-ray energies and multiplicities. To mitigate this dependency, neutron capture measurements with C_6D_6 detectors are analyzed using the TED technique, for which the PHWT must be applied, as explained in detail in Sec. III A. The resulting expression for the capture yield can be written as

$$Y(E_n) = \frac{f_{\rm corr}}{\rm AN}\frac{C_w(E_n) - B_w(E_n)}{\phi_n(E_n)\left(S_n + E_n\frac{A}{A+1}\right)}, \tag{1}$$

where $C_w(E_n)$ is the weighted number of counts in the detector, $B_w(E_n)$ is the weighted number of total background counts, S_n is the neutron separation energy, $\phi_n(E_n)$ is the evaluated flux, A is the mass number of the target nucleus, AN is a normalization factor independent of neutron energy and $f_{\rm corr}$ encompasses different corrections factors that must be applied to enhance the precision, sensitivity, and accuracy of capture yield measurements. A detailed explanation of the data reduction procedure is addressed in the following sections. Particular care has been taken to the detector energy calibration and resolution (Sec. III B), time-of-flight to energy conversion (Sec. III D), background subtraction (Sec. III E), and the correction and normalization factors (Secs. III C and III F, respectively) which affect also the final uncertainty.

A. Total energy detection technique

The TED technique employed in this work is based on two conditions [34,43]:

(1) The first condition imposes that at most one γ ray from the capture event is detected. If this is accomplished, the total efficiency for detecting a cascade, ε_c, can be expressed as

$$\varepsilon_c = 1 - \prod_j \left(1 - \varepsilon_j^\gamma\right) \approx \sum_{j=1}^{N} \varepsilon_j^\gamma, \tag{2}$$

where N is the number of γs emitted in each capture event.

(2) The second condition establishes a proportionality between the detection efficiency and the energy of the γ ray, i.e., $\varepsilon_j^\gamma = \alpha E_j^\gamma$, where usually $\alpha = 1$ by convention. Thus, we have

$$\varepsilon_c \approx \sum_{j=1}^{N} \varepsilon_j^\gamma = \sum_{j=1}^{N} E_j^\gamma = E_c. \tag{3}$$

Therefore, ε_c depends solely on the total energy of the cascade, E_c, and hence it is independent of the de-excitation path and the energy of the detected γ ray. The first condition can be easily fulfilled by employing a low-efficiency detection system (i.e., $\varepsilon^\gamma \ll 1$), while the proportionality condition presents a challenge. For any detection system, the efficiency for γ ray depends on the energy. To meet the proportionality condition needed for the TED technique, the detector response requires a mathematical treatment. This is achieved through the use of the weighting function (WF), which assigns a weight to each deposited energy in such a way that

$$\varepsilon_w^\gamma = \sum_{i=1}^{N} W_i R_i^\gamma = E^\gamma, \tag{4}$$

where R_i^γ is the discretized detector response function to a γ ray of energy E^γ, where $i=1,...,N$ is the number of bins of R_i^γ. This is known as the pulse height weighting technique [34,35] and it is conventionally used in the analysis of neutron-capture cross section at n_TOF [35,36].

The WF was obtained by means of detailed Monte Carlo (MC) simulations [35], which were performed with the Geant4 simulation toolkit [44,45]. A comprehensive model of the entire EAR1 bunker geometry was included in the simulations, encompassing detailed representations of the samples, as well as the experimental self-shielding effect. Simulations were conducted for 120 different monoenergetic γ rays, spanning from 10 keV to 8 MeV, for both the ^{176}Yb and ^{197}Au samples. This broad energy range ensures comprehensive computation of the WF, considering the neutron energy separation values of 5.566 MeV and 6.512 MeV for ^{176}Yb + n and ^{197}Au + n, respectively. The corrections and systematic uncertainties associated to this technique are discussed in the following sections.

B. Detector energy calibration and resolution

The use of PHWT requires precise energy calibration because the pulses are weighted according to their deposited energy. To achieve it, three radioactive sources were measured weekly during the experimental campaign: a ^{137}Cs source emitting a γ ray of 662 keV, a ^{207}Bi source emitting two γ rays of 569 and 1063 keV, and a AmBe source producing a γ-ray energy of 4.438 MeV due to the ^{9}Be(α, n) reaction. Additionally, the deposited energy spectrum of the ^{197}Au(n,γ) reaction, with neutron separation energy of 6.512 MeV [46], was also employed for calibration purposes. The gold capture cascade was used to ensure an accurate calibration at higher energies, taking into account that the neutron separation energy of the capture in ^{176}Yb is at 5.566 MeV [46].

As the response of C_6D_6 detectors lacks a photopeak and instead shows a broad compton edge, the most accurate assessment of energy calibration is by means of simulations. In addition, the energy resolution of the detector is crucial to determine realistic instrumental broadening, which is then applied to the ideal detector response from MC simulations for calculating the WF. Dedicated MC simulations were conducted using the Geant4 toolkit [44,45]. The deposited energy spectra obtained from the simulation output were convoluted with a Gaussian and fitted to the experimental data to reproduce the measurements. The final calibration parameters were determined by the best matching between measured and simulated spectra for each detector individually. An example of the simulated spectrum with and without detector response for one detector is compared to the experimental spectrum in Fig. 3 for the ^{137}Cs source and the deposited energy spectrum of the second γ ray emitted (806 keV) of the ^{207}Bi. It is worth noting that by performing regular calibrations the gain stability of the C_6D_6 detectors could be monitored during the whole measurement. Any gain shift observed was corrected by applying a time-dependent calibration using the periodic calibration runs as reference.

C. Corrections to the detection efficiency

There are several important experimental effects that can affect the detection efficiency. Although the impact of these effects cannot be directly measured, one can exploit the proportionality between the weighted cascade detection efficiency ε_w^c and E_c [Eq. (3)] to estimate corrections for effects such as:

(i) Low signal amplitude threshold. The counts lost when γ rays deposit energy below the experimental detection threshold, f^{th}. The experimental detection threshold has been applied at 200 keV.

(ii) The γ-ray summing. The possible detection of two or more γ rays in coincidence from the same cascade events, f^{sum}.

(iii) Electron correction emission. The probability of internal conversion leading to the emission of electrons instead of a low-energy γ ray, f^{ce}.

The capture γ-ray de-excitation cascades were calculated with the NuDEX code [47]. NuDEX enables the modification of various parameters and statistical models to achieve the most accurate cascades. The output cascades generated by NuDEX are used as input for the Geant4 application developed to simulate the detector response for the PHWT. By comparing the results with the deposited energy spectrum in a particular capture resonance, one can validate the cascade

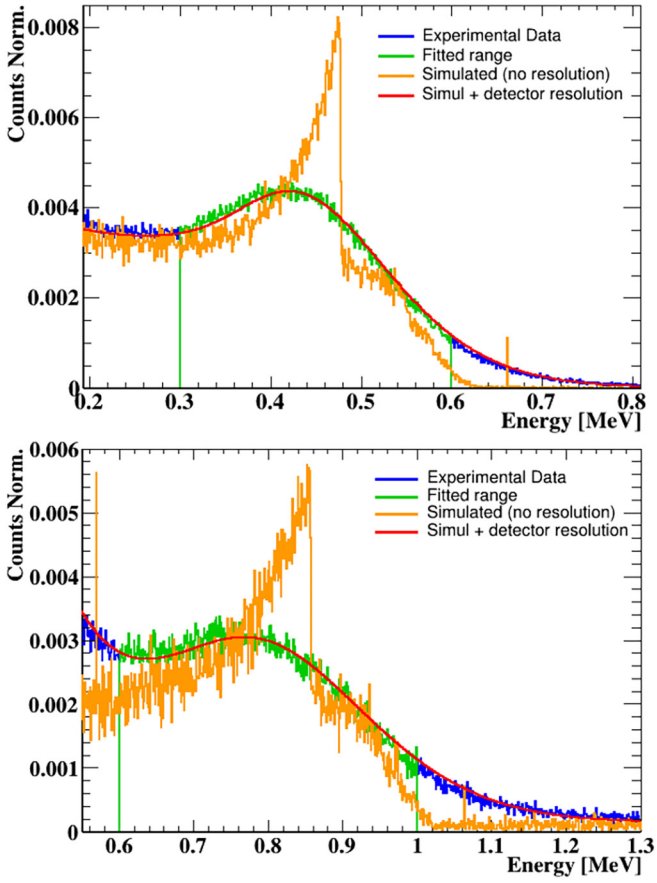

FIG. 3. Deposited energy spectra of the ^{137}Cs source (Top panel) and of the second γ ray emitted (806 keV) of the ^{207}Bi (Bottom panel) in one detector. The experimental data (in blue) is compared to the MC simulation without (orange) and with (red) detector resolution. The green line depicts the energy range employed for the calibration fit. The four spectrum have been normalized to the area of the fitted range.

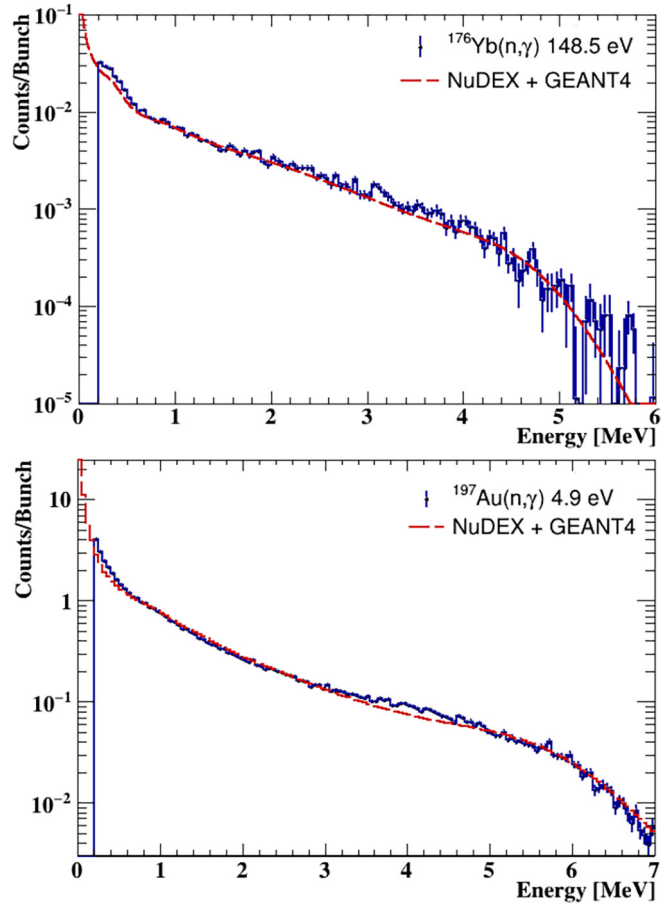

FIG. 4. Top: Energy deposited spectra in the C_6D_6 (blue line) in the strongest resonance of the ^{176}Yb(n,γ) reaction, 148.5 eV, compared to the simulated spectrum (red line). Bottom: Energy deposited spectra in the C_6D_6 (blue line) at 4.9 eV neutron energy for the ^{197}Au(n,γ) reaction compared to the simulated response (red line). The missing low-energy part of the experimental spectrum is corrected via $f_{\rm thr}$ obtained from the simulations.

model employed as input. Additionally, to account for potential variations in the deposited energy spectra between both ^{176}Yb(n,γ) and ^{197}Au(n,γ) reactions, the cascades have been simulated for each sample separately. A comparison between simulated and experimental capture cascades is shown in Fig. 4.

In practice, there is a 6.4 s isomer in ^{177}Yb at 331 keV that decays to the ground state with γ emissions of 104 keV and 227 keV. *For the use of the PHWT, it is important to note how the isomer in the decay path has been handled.* The output from NuDEX gives the time of each transition, allowing the assessment of the influence of the isomer state by comparing simulations that account for the isomer state with those that do not. Moreover, in our particular case, the maximum deposited energy both these γ rays remain below the deposited energy threshold; therefore, the correction due to the isomer is included in the $f^{\rm th}$ correction.

The simulations of the capture cascades can be used to quantify a global correction factor $f_{\rm th,sum,ce}$ by exploiting the principles of the PHWT [Eqs. (3) and (4)] in the following way:

$$f_{\rm th,sum,ce} = \frac{\Sigma_{i=0}^{\infty} W_i R_i^C}{\Sigma_{i=\rm th}^{\infty} W_i R_i^{C,\rm sum,ce}}. \quad (5)$$

Here $R_i^{C,\rm sum,ce}$ and R_i^C are the simulated detector response with and without taking into account the experimental effects, respectively.

Since absolute yield normalization is performed to ^{197}Au, the global correction factor ($f_{\rm corr}$) to the yield is the ratio between those of ^{176}Yb and ^{197}Au, exhibiting agreement within 1% between detectors, and thus this figure has been adopted as the systematic uncertainty for these corrections. The global correction factor for each detector, evaluated for both ^{176}Yb and ^{197}Au, are reported in Table II.

In addition, the simulation of the capture cascades allows to evaluate the goodness of the WF following the conditions specified by Eqs. (3) and (4). Any deviation from unity in the ratio between the weighted response of the detectors and the total energy of the cascade is considered as the uncer-

TABLE II. Corrections factors applied to each detector for obtaining the final yield of the ^{176}Yb(n,γ) reaction.

Detector	$f^{\mathrm{Au}}_{\mathrm{th,sum,ce}}$	$f^{\mathrm{Yb}}_{\mathrm{th,sum,ce}}$	f_{corr}
C_6D_6 #1	1.029(3)	1.059(4)	1.029(7)
C_6D_6 #2	1.042(4)	1.086(5)	1.042(10)
C_6D_6 #3	1.032(4)	1.076(5)	1.043(10)
C_6D_6 #4	1.046(5)	1.089(5)	1.041(10)

tainty in applying the PHWT. The uncertainties range between 0.4–0.7% and 0.3–0.9% for the ^{176}Yb and ^{197}Au samples, respectively. The final uncertainty in the capture yield ascribed to the WF itself is of 1%.

D. TOF to energy conversion

The time taken by neutrons to travel from the production point to the detector serves as the physical observable measured at n_TOF. Neutrons are generated through a spallation process and subsequently moderated, therefore, the relationship between neutron energy and time is not straightforward. Neutrons of the same energy may reach the detector at different times, and various factors contribute to the variation in arrival times [26]. Then, making use of the nonrelativistic formula, the neutron energy corresponding to a specific arrival time at detector is calculated by

$$E_n = \frac{1}{2} m_n \left(\frac{L_0 + \lambda(E_n)}{t_{\mathrm{TOF}} - t_0} \right)^2, \tag{6}$$

where m_n represents the neutron mass, L_0 is the flight path from the center of the target to the experimental area, t_{TOF} is the signal time, t_0 is the time the neutron is produced (calculated from the arrival of the γ flash to each detector, that is, $t_0 \approx t_\gamma - L_0/c$), and $\lambda(E_n)$ is an energy-dependent equivalent moderation length or the resolution function (RF) of the facility. The RF characterizes the distribution of arrival times for neutrons with the same E_n. It is noteworthy that the average of the RF distribution exhibits only slight variations with neutron energy of our interest, and its effects are incorporated into the R-matrix analysis (more details are provided in Sec. IV). The value of the flight path, $L_0 = 184.139(8)$ m, was obtained by a minimization procedure involving the use of the well-known low-energy ^{197}Au(n,γ) resonances retrieved from the JEFF-3.3 evaluation below 100 eV [23].

E. Background analysis

A significant portion of the detected γ rays does not originate from the ^{176}Yb(n,γ) reaction. It is crucial to carefully evaluate and subtract these undesired background signals for an accurate calculation of the capture yield. The background components can be classified according to their origin: *Those unrelated to the sample can be directly measured, while those produced by the sample cannot and must be assessed using ancillary measurements.*

The main contribution to the background arises from the quartz cuvette (as reflected in Fig. 5) and it can be readily measured and subtracted. Other background contributions

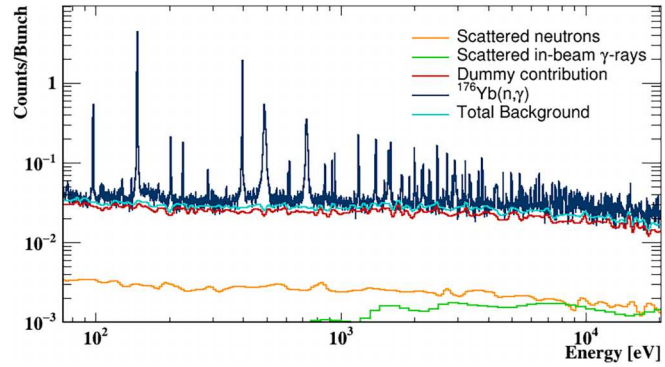

FIG. 5. Neutron energy spectrum of the ^{176}Yb(n,γ) reaction and the total background contribution, including all individual background components. The blue line represents the ^{176}Yb(n,γ) spectra, displayed with 5000 bins per decade; the background components are displayed with 500 bins per decade.

were at most an order of magnitude lower, and were related to in-beam γ rays and neutron scattering in the sample itself which needed thorough assessment. The $^{\mathrm{nat}}C$ sample is essentially a pure neutron scatterer, and hence it was used to evaluate the γ-ray background produced from the secondary capture of neutrons scattered in the sample. However, due to its high Z and high density the ^{208}Pb was used to estimate the background from the scattering of in-beam γ rays.

Considering that in-beam γ rays contribute mainly above $E_n \sim 1$ keV, with negligible contribution below 200 eV, the $^{\mathrm{nat}}C$ is then normalized to the lead between 10 eV and 50 eV. Following this procedure, the $^{\mathrm{nat}}C$ was subtracted from the ^{208}Pb counts, leaving only the in-beam γ-rays contribution. Consequently, we now have well-separated in-beam γ-ray and neutron-scattering contributions, each of which can be scaled and assessed independently [48–50].

The in-beam γ-ray component had to be scaled by a factor accounting for the different Z and density of the Yb sample compared to lead. This factor, k_γ, was extracted by simulating the interaction of the in-beam γ rays in both samples.

However, to properly estimate the neutron-scattering component for the ^{176}Yb, the $^{\mathrm{nat}}C$ spectrum had to be scaled by a factor k_n, expressed as

$$k_n = \frac{n_X}{n_C} \frac{\sigma^X_{\mathrm{el}}}{\sigma^C_{\mathrm{el}}}, \tag{7}$$

where n_X is the areal density of the samples, and σ^X_{el} is the elastic cross section of the different isotopes. The resulting scale factors for each detector and each sample are summarized in Table III.

TABLE III. In-beam γ-ray and neutron-scattering scale factor calculated in this work for each sample.

Sample	k_γ	k_n
^{197}Au	0.0086(5)	0.027(3)
^{176}Yb	0.0971(6)	0.087(4)

After including the in-beam γ-rays and neutron-scattering contributions to the background coming from the quartz cuvette, the total background matched the ^{176}Yb(n,γ) counting rate spectrum between isolated resonances. The different background contributions and the counts from the ^{176}Yb(n,γ) reaction are displayed in Fig. 5. Nevertheless, the residual background that can remain was assessed by using the SAMMY code which can also take into account the systematic uncertainties. The evaluation of the later uncertainties has been carried out using different residual backgrounds and assessing their impact on the calculated resonance parameters (more details in Sec. IV A).

F. Normalization and systematic uncertainties discussion

The absolute normalization factor (AN), presented in Eq. (1), represents the fraction of the neutron beam intercepting the sample and the absolute neutron flux normalization. This was calculated, individually for each detector, by means of the aforementioned saturated resonance method (SRM) [32]. This method ensures proper normalization of the measured reaction rates, thereby mitigating the impact of uncertainties in detection efficiency and simulation, canceling out any difference between the experimental setup and the simulated one.

The SRM consists of employing a reference sample with a neutron resonance where the dominant reaction mechanism is capture, and its peak capture cross section σ_γ is very high. If the sample is thick enough, then all neutrons near the E_r will be captured, and hence the yield will be close to 1 (i.e., "saturation"), as long as the sample covers the entire neutron beam. In this work the well-known 4.9 eV resonance of ^{197}Au was employed. The normalization sample had the same diameter as the ^{176}Yb-enriched sample (19 mm) and a thickness of 50 μm. AN was determined by fitting the 4.9 eV resonance with the R-matrix code SAMMY [51], with an associated uncertainty of less than 0.1%. The fit of the 4.9 eV resonance is depicted in Fig. 6 for the ^{197}Au sample. AN was also obtained for a ^{197}Au sample big enough to cover the full beam. The ratio of the two normalization factors provided an experimental value of the beam intersection factor (BIF) for the 19 mm samples, accounting for the geometrical alignment and spatial distribution of the neutron beam and the target.

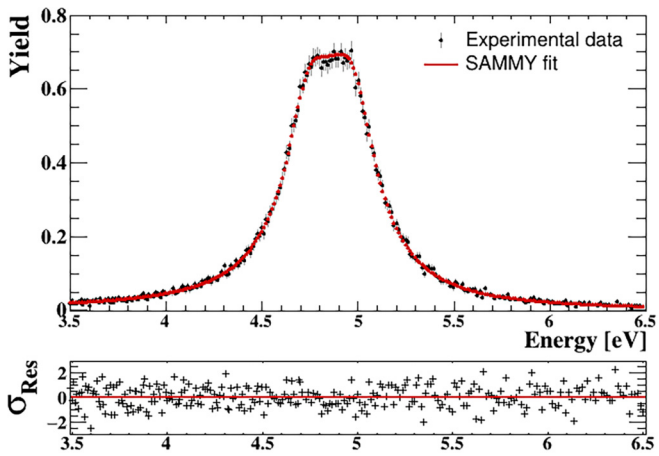

FIG. 6. ^{197}Au(n,γ) reaction yield for the C_6D_6 #1, represented by black points, along with the R-matrix fit performed using SAMMY, indicated by the red line, in the saturated resonance at 4.9 eV.

TABLE IV. The absolute normalization factor AN presented for each detector obtained from the fit of ^{197}Au saturated resonance at 4.9 eV, in addition to the BIF. The uncertainties in the table arise from the uncertainty in fitting the saturated resonance and the counting statistics.

Detector	AN	BIF
C_6D_6 #1	0.702(6)	0.617(10)
C_6D_6 #2	0.742(7)	0.622(10)
C_6D_6 #3	0.782(8)	0.619(12)
C_6D_6 #4	0.804(9)	0.619(12)

The values of the BIF for the four detectors agree with each other within 1%, which is thereby assumed as the systematic uncertainty for the absolute normalization. Values of AN and BIF are summarized in Table IV.

It is worth noting that the relative positioning between the Au sample and the Yb sample is known with a precision of ±1 mm. This uncertainty corresponds to a 1.5% of systematic uncertainty in the ^{176}Yb yield determination, assessed by means of simulations. The systematic uncertainties from different sources contributing to the resulting yield are summarized in Table V. The resulting quadratic sum of partial systematic uncertainties in the ^{176}Yb yield is ∼3.4%.

IV. RESONANCE ANALYSIS

The resonance analysis of ^{176}Yb(n,γ) was performed with the Bayesian code SAMMY [51]. SAMMY utilizes the R-matrix formalism for analyzing experimental data from time-of-flight experiments, employing the Reich-Moore approximation. Additionally, SAMMY incorporates corrections for various experimental conditions, including Doppler and resolution broadening, multiple-scattering corrections for capture yields, multinuclide samples, and backgrounds.

TABLE V. Systematic uncertainties due from different sources in the measurement of ^{176}Yb(n,γ) reaction.

Source of uncertainty	σ_{sys} (%)
Beam stability	1
C_6D_6 Gain Shift	1
PHWT (Efficiency)	1
Capture Cascade Correction Factors	1
Relative position Au/Yb	1.5
Neutron Flux	2
Absolute Normalization	1
Total (Capture Yield)	∼3.4

A. Individual resonances parameters

This work reports the first measurement of the ^{176}Yb(n,γ) reaction resolving resonances. Also, two transmission measurements from 1970s were performed and resolved resonances. The first one, performed by Mughabghab and Chrien [20] in 1968, in the Brookhaven Graphite Research Reactor at Brookhaven National Laboratory, measured seven resonances in the E_n range between 140 eV and 3 keV, albeit with significant uncertainties in the resonance parameters. A subsequent transmission measurement in 1973 by Liou *et al.* [19] expanded the number of known resonances to 68 up to 20 keV. The resonance parameters reported in this reference have been taken as the basis for this work, along with the parameters compiled in ENDF/B-VIII.0 [21] and JEFF-3.3 [23], the latter extending up to 26 keV. The spin group for the known resonances were taken from the "Atlas of Neutron Resonances" by Mughabghab [10].

A total of 164 resonances were resolved and analyzed in the present work in the E_n below 21 keV. First, an in-depth examination of the residual background was undertaken, and its influence on the resonance parameters was evaluated. The impact has been carried out fitting the resonance parameters considering different residual backgrounds, found minor differences between them. Afterwards, the contamination from very low quantities of the other Yb isotopes was considered. Their corresponding abundances were fitted with SAMMY, using observed resonances considering their parameters from ENDF/B-VIII.0. The contributions from the Yb isotopes are summarized in Table I.

The resonance analysis is adapted according to whether the resonance had been measured in earlier transmission experiments or not. If reported from transmission, the procedure involved initially fixed Γ_n at value from Mughabghab [10], and determining the resonance energy (E_r) with the fit, then, adjusting the Γ_γ, and then try to fit also Γ_n within a range. In resonances exhibiting similar decay widths, or discrepancies in the spin assignment across different references, it was convenient to explore potential correlations between Γ_γ and Γ_n. This was achieved by plotting the reduced χ-squared (χ^2) values for various combinations of Γ_γ and Γ_n within an extensive range, as it is displayed in Fig. 7.

The corresponding R-matrix fit for the first resonances are displayed in Figs. 8 and 9. The new results are compared to the yield calculated with parameters extracted from the ENDF/B-VIII.0 [21] and JEFF-3.3 [23] evaluations. In addition, a comparison with the yield expected from previous transmission experiments is shown.

The second case, when the resonance was not resolved in transmission experiments, the criteria employed for identifying a new resonance at a certain E_n was that a peak must encompass at least three consecutive points deviating more than $2\sigma_{\text{res}}$ from the background level at low E_n, while at energies higher than 10 keV, two such points were deemed sufficient for resonance identification. For fitting these new resonances, where no prior information existed, we use as initial input parameter the $\langle\Gamma_\gamma\rangle = 60.5$ meV provided by Mughabghab [10].

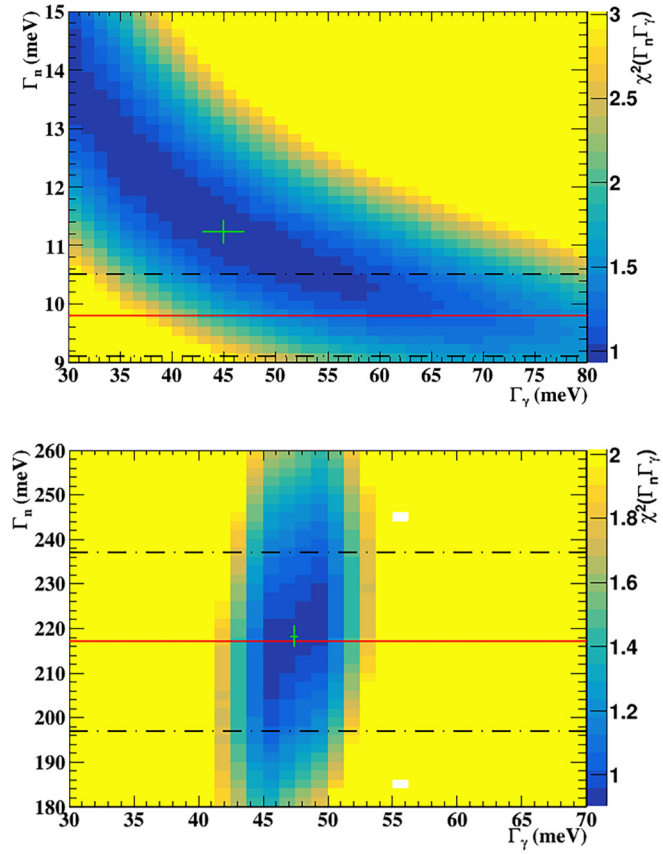

FIG. 7. Two-dimensional plot of the reduced χ^2 as a function of the resonance parameters Γ_n and Γ_γ. In green, the best value obtained through the fit is displayed, in comparison with the Γ_n parameter reported by Liou *et al.*, displayed with a red line, and the corresponding errors with a dashed black line. $E_r = 148.5$ eV (up) and $E_r = 398$ eV (bottom), respectively.

The excellent resolution in neutron energy of EAR1 combined with the high statistics of our experimental data have led to an increase in the number of reported resonances to 164, *a considerably larger number than from the previous transmission measurements.* In Fig. 10 we show the experimental yield with the corresponding R-matrix fit for several neutron energy regions. Our results are compared to the yield calculated with parameters extracted from the ENDF/B-VIII.0 [21] and JEFF-3.3 [23] evaluations.

Finally, the systematic uncertainties are summarized in Table VI. An additional uncertainty of 2% and 3% related to the sample mass and the background component, respectively,

TABLE VI. Evaluation of the primary sources of systematic uncertainties in the measurement of ^{176}Yb(n,γ).

Systematic uncertainty	σ_{sys} (%)
Total (Capture Yield)	<3.4
Background	3
Sample mass uncertainty	2
Total (Resonance parameters)	<5.1

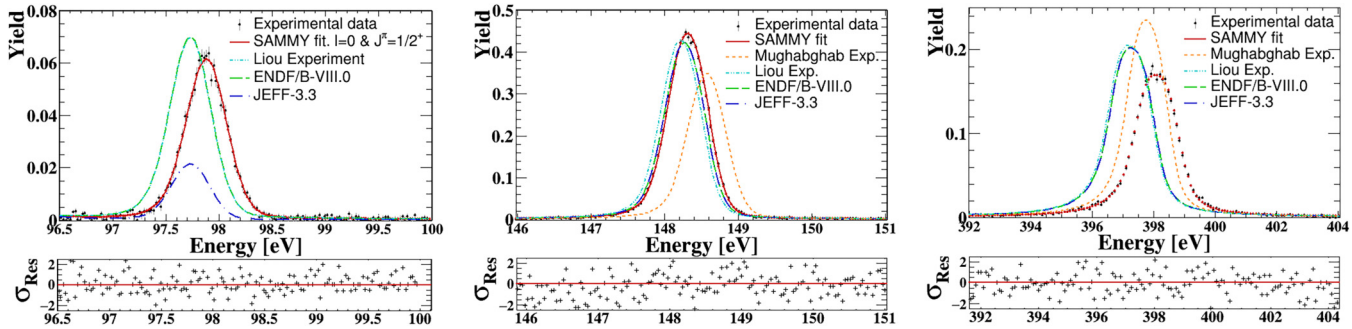

FIG. 8. Capture yield obtained in this work (dark markers) with the corresponding SAMMY fit (red markers), compared with the yield, for individual resonances, extracted from the previous experiments of Mughabghab and Chrien (orange line) and Liou *et al.* (light blue line), and the capture yield extracted from the ENDF/B-VIII.0 (green line) and JEFF-3.3 (dark blue line) evaluations.

have been considered in the resonance analysis, for extracting the resonance decay widths. Further, although the setup was optimized to minimize the impact of neutron sensitivity, the resonance parameters of certain resonances with high Γ_n/Γ_γ ratio could be affected by such neutron sensitivity. Once the R-matrix analysis was completed, the impact of neutron sensitivity was evaluated. The results obtained in this work show that this impact is negligible and hence the uncertainty due to this is not included in the final results.

B. Resonance parameters of the ^{176}Yb(n,γ) reaction

The result of our analysis is compared with previous transmission experiments works and evaluations. This comparison has been performed in terms of the radiative kernel of the resonances, R_k, calculated from the resonances parameters as

$$R_k = g_J \frac{\Gamma_\gamma \Gamma_n}{\Gamma_\gamma + \Gamma_n}, \tag{8}$$

where g_J is the spin factor defined as $g_J = \frac{(2J+1)}{(2I+1)(2i+1)}$, where $i = 1/2$ and $I = 0$ are the spins of the neutron and the target nucleus, respectively, and J is the angular momentum of the resonances. Regarding the spin of the resonances, we have used the J^π provided by Mughabghab [10]. For new resonances, we have selected the J^π which provides the best fit of the resonance below 2 keV, *above this energy the* J^π *has been assumed as s-wave*. Nonetheless, it appears that kernels and individual widths obtained with different assumptions on

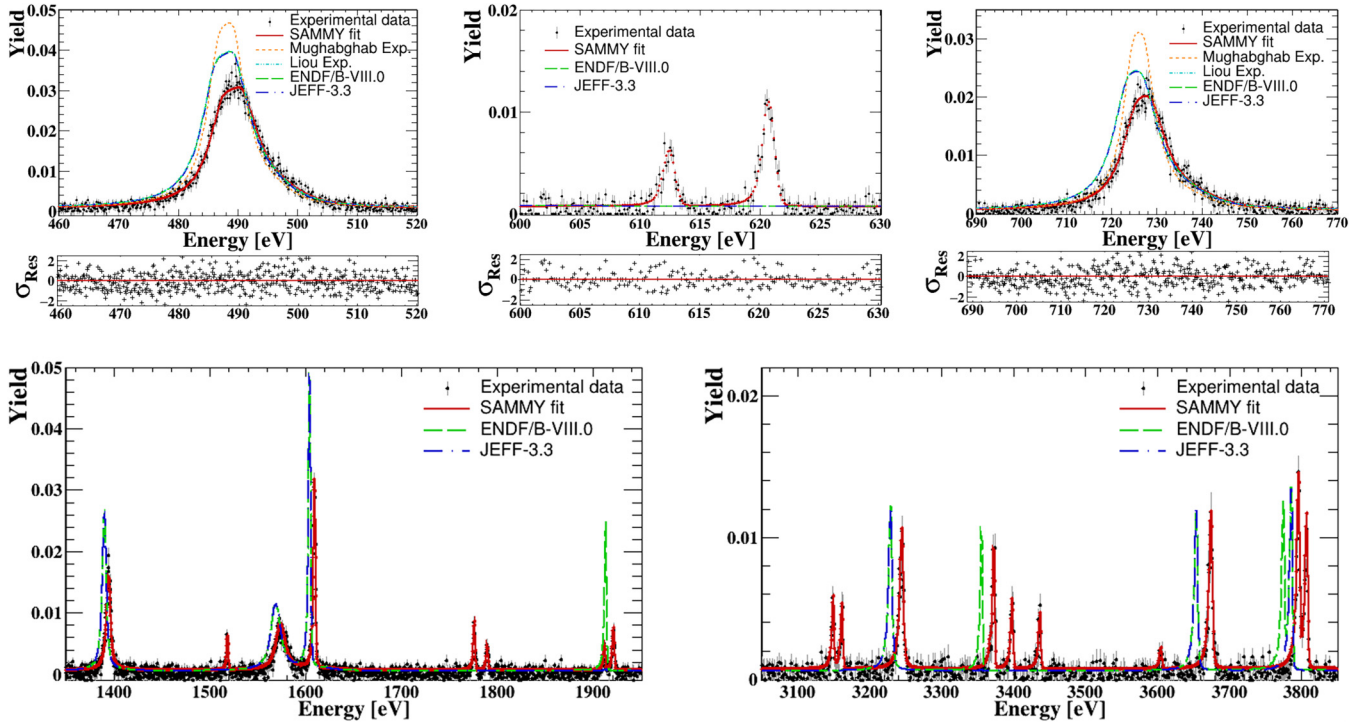

FIG. 9. The experimental capture yield from this work (dark markers) with the corresponding SAMMY fit (red markers), compared to the yield calculated using parameters from the ENDF/B-VIII.0 (green dashed line) and JEFF-3.3 (dark blue dash-dotted line) evaluations. For some resonances the results are also compared to the yield calculated with parameters from previous experiments (see text for details).

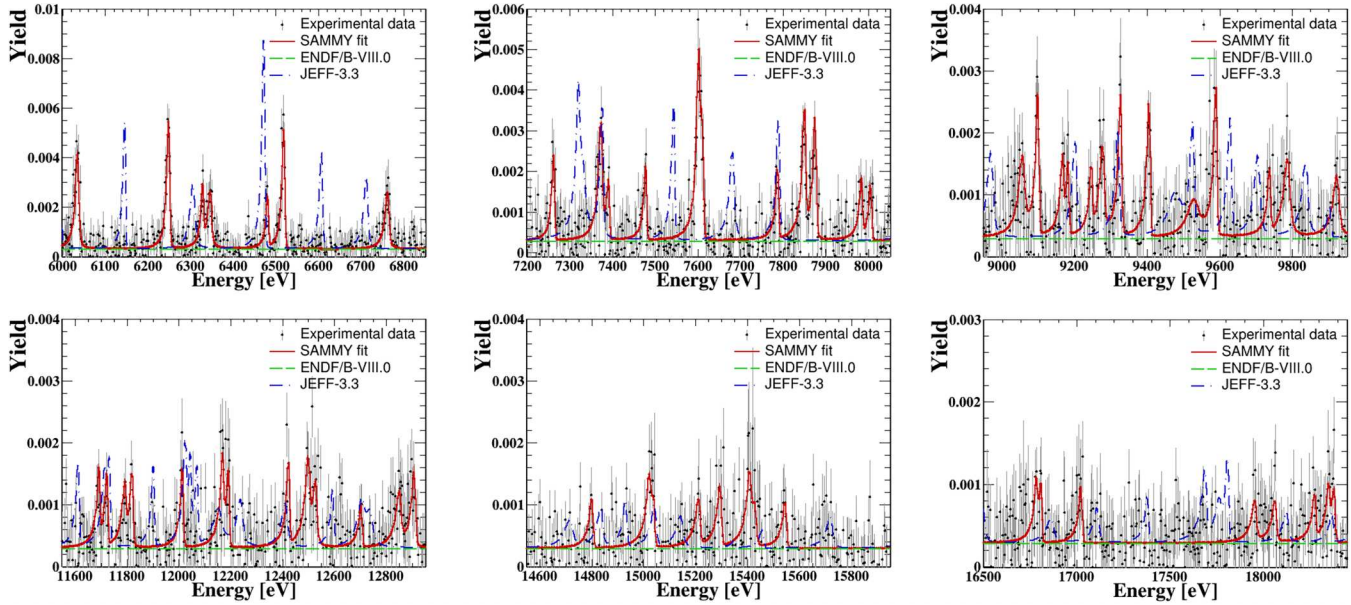

FIG. 10. The experimental capture yield from this work (dark markers) with the corresponding SAMMY fit (red markers), compared to the yield calculated using parameters from the ENDF/B-VIII.0 (green dashed line) and JEFF-3.3 (dark blue dash-dotted line) evaluations.

resonance spin and parity are not affected. Table VII of the Appendix shows our result of the resonance parameters.

The ratio between the kernels obtained in this work and the kernels calculated using the Γ_n parameter reported by Liou *et al.* and Mughabghab and Chrien and fixing Γ_γ are shown in Fig. 11. Since the two transmission measurements only reported Γ_n values, to calculate the kernels for all resonances Γ_γ was set to the average value of $\langle\Gamma_\gamma\rangle = 60.5(3.4)$ meV provided by Mughabghab. Due to the high resolution reached in our experiment, at high energies some of the individual resonances identified by Liou *et al.* have been identified as multiplet structures, therefore, we restrict the comparison up to 10 keV. The comparison with the libraries has not been presented since the parameters are the same as those given by Liou *et al.* and those reported in Mughabghab.

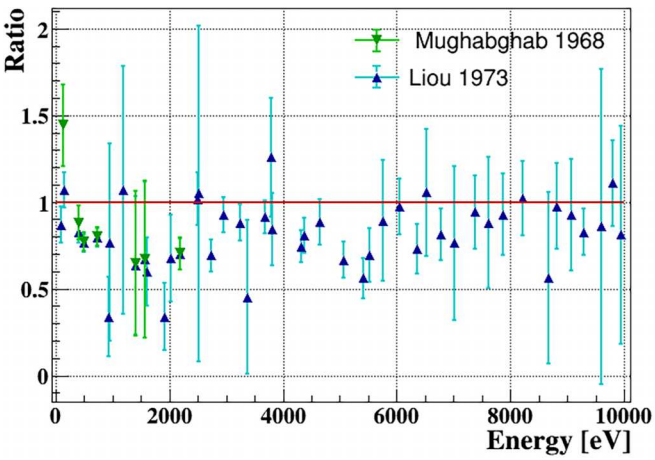

FIG. 11. Ratios between the resonance kernels obtained in this work and those reported by Liou *et al.* and Mughabghab and Chrien.

On one side, the comparison between this work and the measurement of Mughabghab and Chrien shows that the average kernel ratio between Mughabghab and Chrien and this work is 0.92(16). However, comparison with Liou *et al.* shows that the ratio between Liou *et al.* and this work is 0.79(37). Considering that Γ_n in this work was taken as a reference from Mughabghab, which is the same one that Liou *et al.* reported in their work, the differences must arise from Γ_γ, which is lower for most of our resonances, than the one assumed for the results of Liou *et al.*

V. CONCLUSIONS

A measurement of the ^{176}Yb(n,γ) reaction was performed successfully at the EAR1 station of the n_TOF facility located at CERN, using an array of four C_6D_6 liquid scintillation detectors. The capabilities of the n_TOF facility, characterized by its high energy resolution, high instantaneous flux and the low background in EAR1, enabled resolving the resonances of the reaction for the first time.

We have obtained the capture yield with a low level of systematic uncertainty, approximately ∼3.4% in the energy range from 90 eV to 21 keV. Once the capture yield was determined, a resonance analysis was conducted using the Bayesian code SAMMY. In this analysis, a total of 164 resonances were resolved up to 21 keV. This represents a significant advancement compared to previous transmission measurements; Mughabghab and Chrien were only able to resolve 7 resonances, while in a posterior measurement Liou *et al.* raised this figure to 68. In our work, we identified 96 new resonances, showcasing the quality of the measurement and the detail of our analysis.

The comparison with the transmission experiments shows some discrepancies in the radiative kernels. These discrepancies arise from the Γ_γ width, *which was not reported in*

such works; meanwhile, it can be accurately determined in our experiment. In most cases, our analysis provides a lower value, than the one reported by Mughabghab up to 10 keV. Above this energy, we did not compare with transmission measurements because some of their individual resonances were clearly identified as multiplets of two or three resonances, thanks to the high resolution of the n_TOF neutron beam.

ACKNOWLEDGMENTS

This work has been carried out within the framework of Project No. PID2020.117969RB.I00 funded by Grant No. MICIU/AEI/10.13039/501100011033. F.G.-I. acknowledges Ph.D. CERN Contract No. TSC-2020-2/DOCT EN-nT2. Support of funding agencies of all institutions participating at n_TOF is acknowledged.

APPENDIX: LIST OF ^{176}Yb(n,γ) RESONANCE PARAMETERS COMPILED IN THIS WORK

TABLE VII. List of the capture resonances of the ^{176}Yb(n, γ) reaction detected in this work. Energy, E_0, Γ_γ and Γ_n are provided for all the resonances measured in this work. The uncertainties listed in the table are only statistical and have been obtained from the SAMMY calculations.

E_0(eV)	J^π	l	Γ_γ (meV)	Γ_n (meV)	R_k (meV)
98.0299(19)	0.5^+	0	53.5(47)	0.473(4)	0.469(4)
148.5448(10)	0.5^+	0	45.0(20)	11.23(18)	8.98(19)
203.337(7)	1.5^-	1	59(27)	0.234(5)	0.466(10)
227.451(7)	1.5^-	1	38(8)	0.256(6)	0.509(13)
289.054(23)	1.5^-	1	40(34)	0.121(6)	0.241(13)
397.719(4)	0.5^+	0	47.4(3)	218.2(24)	39.0(3)
489.641(19)	0.5^+	0	46.0(4)	2622(20)	45.2(4)
613.38(4)	1.5^-	1	46(34)	0.700(38)	1.37(8)
621.67(3)	0.5^-	1	48(24)	1.39(5)	1.35(7)
728.031(37)	0.5^+	0	48.0(5)	3881(45)	47.4(5)
865.36(3)	1.5^-	1	75(51)	1.29(5)	2.53(13)
928.32(3)	1.5^-	1	62(54)	1.47(5)	2.87(15)
953.25(2)	1.5^-	1	40(40)	2.65(15)	4.9(6)
1185.44(6)	1.5^-	1	65(33)	7.2(2)	12.9(10)
1196.237(7)	0.5^+	0	43(32)	2.03(2)	1.94(25)
1396.94(18)	0.5^+	0	37.9(22)	2130(74)	37(21)
1520.91(13)	0.5^+	0	43(41)	1.80(16)	1.7(15)
1576.4(4)	0.5^+	0	40.3(25)	5750(580)	40(25)
1611.7(5)	0.5^+	0	35.1(10)	410(41)	32(9)
1778.641(9)	1.5^-	1	43(4)	3.5(4)	6.5(7)
1792.1(3)	1.5^-	1	43(4)	1.68(17)	3.2(3)
1913.91(3)	1.5^-	1	59(59)	1.94(19)	3.8(5)
1924.038(25)	1.5^-	1	59(59)	3.5(3)	7(1)
2016.8(1.3)	0.5^+	0	40.4(13)	1120(101)	38(12)
2025.5(3)	0.5^+	0	59(52)	8.9(8)	7.7(15)
2073.75(3)	0.5^+	0	59(6)	3.7(4)	3.5(4)
2156.39(7)	0.5^+	0	60(60)	14(4)	11(5)
2188.77(32)	0.5^+	1	42(3)	3037(210)	41(3)
2306.49(9)	1.5^-	1	58(51)	10(9)	17(15)
2335.5(19)	1.5^-	0	59(59)	0.54(25)	1.1(5)
2346.19(3)	0.5^+	0	59(59)	12.5(10)	10(2)
2497.73(17)	0.5^+	0	61(3)	331(73)	52(4)
2520.878(9)	1.5^-	1	59(57)	17(6)	26(13)
2646.08(1)	0.5^+	1	50(50)	3.14(15)	2.9(3)
2733.5(5)	0.5^+	0	40.0(22)	471(114)	36(3)
2875.165(9)	1.5^-	1	60(44)	26(18)	36(25)
2937.1(4)	0.5^+	0	59(59)	3.7(7)	3.5(8)
2945.8(2.6)	0.5^+	0	56(3)	8019(632)	55(3)
2981.1(10)	0.5^+	0	59(55)	14(3)	11(4)
3008.82(8)	0.5^+	0	60(59)	11.3(16)	9(3)
3154.1(3)	0.5^+	0	59(57)	15(4)	12(5)
3166.22(16)	0.5^+	0	59(55)	14(3)	11(4)

TABLE VII. *(Continued.)*

E_0(eV)	J^π	l	Γ_γ (meV)	Γ_n (meV)	R_k (meV)
3250(2)	0.5^+	0	53(3)	1903(260)	52(3)
3372.0(23)	1.5^-	1	60(60)	1.0(10)	2(2)
3378.23(4)	0.5^+	0	63(52)	15(8)	12(7)
3403.32(7)	0.5^+	0	59(58)	18(6)	14(7)
3441.592(9)	0.5^+	0	59(59)	14(4)	11(5)
3609.84(7)	0.5^+	0	59(58)	4.9(17)	5(2)
3680.50(25)	0.5^+	0	55(2)	1243(280)	52(2)
3802.1(3)	0.5^+	0	68(4)	185(92)	50(9)
3813(3)	0.5^+	0	50(5)	460(420)	45(8)
3930.061(13)	0.5^+	0	59(59)	11(3)	9(4)
4271.31(23)	0.5^+	0	60(60)	24(9)	17(10)
4327.0(8)	0.5^+	0	44(3)	5837(610)	44(3)
4375(5)	0.5^+	0	47(3)	4268(610)	46(3)
4647.7(25)	0.5^+	0	53(3)	733(380)	49(4)
4790.81(15)	0.5^+	0	60(60)	19(5)	14(6)
4815.3(8)	0.5^+	0	60(60)	14(4)	11(5)
5070.6(12)	0.5^+	0	40(4)	3052(800)	39(4)
5233.84(8)	0.5^+	0	60(60)	29(29)	20(20)
5334.4(4)	0.5^+	0	59(59)	30(6)	20(9)
5418.2(15)	0.5^+	0	34(5)	4097(1600)	34(5)
5442.9(24)	0.5^+	0	42(4)	1415(800)	41(4)
5507.16(16)	0.5^+	0	55(55)	6.2(62)	6(6)
5517.4(19)	0.5^+	0	41(4)	615(611)	38(6)
5600.88(10)	0.5^+	0	59(57)	31(16)	20(13)
5753(10)	0.5^+	0	54(18)	23 013(14000)	54(17)
5854.12(21)	0.5^+	0	60(60)	27(9)	19(10)
5985.5(28)	0.5^+	0	60(56)	35(17)	22(14)
6044(5)	0.5^+	0	59(6)	3241(1500)	58(6)
6257.9(8)	0.5^+	0	64(5)	1059(760)	60(7)
6337.80(12)	0.5^+	0	56(56)	36(18)	22(15)
6355.8(11)	0.5^+	0	44(6)	5030(2100)	44(6)
6489.40(8)	0.5^+	0	60(60)	32(12)	21(12))
6528.9(12)	0.5^+	0	63(14)	770(770)	58(16)
6773.3(12)	0.5^+	0	49(6)	4220(2300)	48(6)
7004(8)	0.5^+	0	46(24)	10 600(8700)	46(24)
7273(4)	0.5^+	0	60(54)	49(38)	27(22)
7384(3)	0.5^+	0	57(9)	2920(1900)	56(9)
7401.66(3)	0.5^+	0	59(59)	29(16)	19(14)
7489.35(3)	0.5^+	0	59(59)	44(35)	25(22)
7613.4(12)	0.5^+	0	59(15)	330(320)	50(18)
7621(3)	0.5^+	0	54(7)	1230(1230)	52(9)
7799.0(5)	0.5^+	0	60(60)	45(28)	26(20)
7862.9(13)	0.5^+	0	56(9)	1460(1460)	54(10)
7887(4)	0.5^+	0	60(8)	1450(1440)	58(10)
7996.2(12)	0.5^+	0	59(59)	34(12)	22(13)
8018(4)	0.5^+	0	60(60)	35(24)	22(18)
8221(4)	0.5^+	0	62(8)	2270(2270)	60(9)
8266(5)	0.5^+	0	49(6)	2100(2100)	48(7)
8343.5(17)	0.5^+	0	60(60)	28(19)	19(14)
8435.5(15)	0.5^+	0	60(7)	930(930)	56(10)
8664(8)	0.5^+	0	34(28)	8780(8500)	34(28)
8737(3)	0.5^+	0	59(59)	34(28)	22(19)
8812(5)	0.5^+	0	59(11)	3400(2500)	58(11)
8900(5)	0.5^+	0	59(59)	34(21)	22(16)
9072(6)	0.5^+	0	56(16)	9000(9000)	56(16)
9113.1(15)	0.5^+	0	60(18)	330(330)	51(21)
9181.2(11)	0.5^+	0	59(59)	34(29)	22(20)

TABLE VII. *(Continued.)*

E_0(eV)	J^π	l	Γ_γ (meV)	Γ_n (meV)	R_k (meV)
9196.1(8)	0.5^+	0	65(55)	41(24)	25(17)
9261(4)	0.5^+	0	50(50)	35(35)	21(21)
9292(7)	0.5^+	0	50(5)	5800(5800)	50(5)
9342(4)	0.5^+	0	59(10)	640(640)	54(12)
9419(3)	0.5^+	0	59(14)	340(340)	50(17)
9590(10)	0.5^+	0	52(52)	26 500(26500)	52(52)
9605.0(16)	0.5^+	0	63(11)	332(33)	53(9)
9753.01(8)	0.5^+	0	61(61)	40(27)	24(19)
9804(4)	0.5^+	0	67(11)	9960(6800)	67(11)
9940(8)	0.5^+	0	49(35)	8900(8900)	49(35)
10 078(4)	0.5^+	0	60(29)	67(67)	32(23)
10 162(4)	0.5^+	0	60(36)	180(180)	45(32)
10 327(5)	0.5^+	0	64(8)	1400(1400)	61(10)
10 403(4)	0.5^+	0	60(31)	100(100)	38(26)
10 605(5)	0.5^+	0	60(33)	1700(1700)	58(32)
10 688(4)	0.5^+	0	60(60)	40(23)	24(18)
10 838(5)	0.5^+	0	60(15)	600(600)	55(17)
10 860(4)	0.5^+	0	60(46)	60(44)	30(23)
11 045(2)	0.5^+	0	60(30)	180(180)	45(28)
11 415(4)	0.5^+	0	60(20)	180(180)	45(23)
11 710(5)	0.5^+	0	48(18)	600(600)	44(19)
11 740(5)	0.5^+	0	52(23)	300(300)	44(23)
11 810(6)	0.5^+	0	46(39)	3500(3600)	45(38)
11 838(5)	0.5^+	0	54(24)	1500(1500)	52(24)
12 033(5)	0.5^+	0	60(27)	500(500)	54(27)
12 189(6)	0.5^+	0	60(20)	1500(1500)	58(21)
12 210(5)	0.5^+	0	60(11)	1100(1100)	57(13)
12 443(8)	0.5^+	0	74(27)	220(220)	55(29)
12 519(8)	0.5^+	0	82(35)	6050(6050)	81(35)
12 548(5)	0.5^+	0	70(17)	6220(6220)	69(17)
12 723(5)	0.5^+	0	44(44)	110(110)	31(31)
12 873(9)	0.5^+	0	66(18)	8560(8560)	65(18)
12 929(6)	0.5^+	0	75(25)	3270(3270)	73(26)
13 155(5)	0.5^+	0	60(55)	270(270)	49(46)
13 400(5)	0.5^+	0	60(24)	370(370)	52(25)
13 560(16)	0.5^+	0	55(45)	25 100(2300)	55(45)
13 775(11)	0.5^+	0	73(33)	12 260(12260)	73(33)
13 948(9)	0.5^+	0	78(21)	8980(8980)	77(21)
14 091(5)	0.5^+	0	59(14)	500(500)	53(17)
14 201(8)	0.5^+	0	60(58)	8900(8900)	60(58)
14 422(5)	0.5^+	0	40(40)	287(287)	35(35)
14 825(5)	0.5^+	0	66(66)	207(207)	50(50)
15 046(6)	0.5^+	0	62(67)	1100(1100)	59(63)
15 062(5)	0.5^+	0	61(24)	1100(1100)	58(25)
15 237(6)	0.5^+	0	61(53)	2530(2500)	60(52)
15 319(5)	0.5^+	0	76(26)	790(790)	69(28)
15 434(6)	0.5^+	0	78(57)	22 340(22340)	78(57)
15 453(7)	0.5^+	0	63(60)	3720(3700)	62(59)
15 571(5)	0.5^+	0	69(48)	223(223)	53(40)
16 263(6)	0.5^+	0	50(50)	1790(1790)	49(49)
16 340(5)	0.5^+	0	80(45)	290(290)	63(41)
16 810(5)	0.5^+	0	62(60)	205(200)	48(46)
16 835(6)	0.5^+	0	71(57)	703(700)	65(53)
17 050(6)	0.5^+	0	70(34)	503(503)	61(34)
17 986(9)	0.5^+	0	70(70)	7500(7500)	69(69)
18 094(9)	0.5^+	0	70(36)	7000(7000)	69(36)
18 306(6)	0.5^+	0	60(60)	500(500)	54(54)

TABLE VII. *(Continued.)*

E_0(eV)	J^π	l	Γ_γ (meV)	Γ_n (meV)	R_k (meV)
18 380(6)	0.5^+	0	60(60)	500(500)	54(54)
18 410(7)	0.5^+	0	80(33)	2000(2000)	77(33)
19 137(6)	0.5^+	0	70(70)	1700(1700)	67(67)
19 233(7)	0.5^+	0	85(42)	1870(1870)	81(41)
19 730(5)	0.5^+	0	60(38)	955(960)	56(37)
19 739(5)	0.5^+	0	59(54)	950(960)	56(51)
19 763(7)	0.5^+	0	55(65)	2640(2500)	54(63)
20 562(6)	0.5^+	0	62(62)	560(560)	56(56)
21 000(6)	0.5^+	0	81(79)	555(550)	71(69)

[1] G. Tessitore, G. A. Mandl, S. L. Maurizio, M. Kaur, and J. A. Capobianco, RSC Adv. **13**, 17787 (2023).
[2] K. Wisshak, F. Voss, C. Arlandini, F. Käppeler, and L. Kazakov, Phys. Rev. C **61**, 065801 (2000).
[3] N. Prantzos, C. Abia, S. Cristallo, M. Limongi, and A. Chieffi, Mon. Not. R. Astron. Soc. **491**, 1832 (2019).
[4] J. J. Cowan, C. Sneden, J. E. Lawler, A. Aprahamian, M. Wiescher, K. Langanke, G. Martínez-Pinedo, and F.-K. Thielemann, Rev. Mod. Phys. **93**, 015002 (2021).
[5] J. Strosberg *et al.*, N. Engl. J. Med. **376**, 125 (2017).
[6] O. Sartor *et al.*, Nucl. Med. Mol. Imag. **46**, 2536 (2019).
[7] K. Ferreira, S. Collins, and A. Fenwick, EPJ Web Conf. **146**, 08002 (2017).
[8] S. Prevot *et al.*, EJNMMI Phys. **10**, 3 (2023).
[9] M. Balzer *et al.*, EJNMMI Radiopharm. Chem. **8**, 37 (2023).
[10] S. F. Mughabghab, *Atlas of Neutron Resonances* (Elsevier Science & Technology, Amsterdam, 2018).
[11] F. Farina Arboccò, P. Vermaercke, K. Smits, L. Sneyers, and K. Strijckmans, J. Radiol. Nucl. Chem. **302**, 655 (2014).
[12] F. De Corte and A. Simonits, Nuclear Data for Science and Technology (1988), pp. 583–586.
[13] R. E. Heft, UCRL-80286(Rev.1); CONF-800477-1; TRN: 80-010581, United States (1980), https://www.osti.gov/biblio/5430238.
[14] J. Alstad, L. Hertzenberg, and A. C. Pappas, Norwegian report to the INDC (International Nuclear Data Committee) (1972), No.1, p.1(2).
[15] D. Stupegia, M. Schmidt, C. Keedy, and A. Madson, J. Nucl. Energy **22**, 267 (1968).
[16] V. S. Shorin, V. N. Kononov, and E. D. Poletaev, Yad. Fiz. **20**, 1092 (1974).
[17] M. V. Bokhovko, V. N. Kononov, E. D. Poletaev, N. S. Rabotnov, and V. M. Timokhov, in *Nuclear Data for Science and Technology*, edited by S. M. Qaim (Springer, Berlin, 1992), pp. 62–64.
[18] J. Marganiec, I. Dillmann, C. Domingo-Pardo, and F. Käppeler, Phys. Rev. C **90**, 065801 (2014).
[19] H. I. Liou, H. S. Camarda, G. Hacken, F. Rahn, J. Rainwater, M. Slagowitz, and S. Wynchank, Phys. Rev. C **7**, 823 (1973).
[20] S. F. Mughabghab and R. E. Chrien, Phys. Rev. **174**, 1400 (1968).
[21] D. Brown *et al.*, Nucl. Data Sheets **148**, 1 (2018).
[22] A. J. Koning, D. Rochman, J.-C. Sublet, N. Dzysiuk, M. Fleming, and S. Van der Marck, Nucl. Data Sheets **155**, 1 (2019).
[23] A. J. M. Plompen, O. Cabellos, C. De Saint Jean *et al.*, Eur. Phys. J. A **56**, 181 (2020).
[24] U. Abbondanno *et al.*, CERN n_TOF Facility: Performance Report, Technical report (CERN, n_TOF-PUB-2010-001, 2003).
[25] Centre Européenne pour la Recherche Nucleaire (2022), https://home.cern/science/accelerators
[26] C. Guerrero *et al.*, Eur. Phys. J. A **49**, 27 (2013).
[27] N. Patronis *et al.*, EPJ Techn. Instrument. **10**, 13 (2023).
[28] E. Chiaveri, Proposal for n_TOF experimental area 2 (EAR-2) (2012), https://cds.cern.ch/record/1411635?ln=es.
[29] C. Weiß *et al.*, Nucl. Instrum. Methods Phys. Res. A **799**, 90 (2015).
[30] N. Colonna, F. Gunsing, and F. Käppeler, Prog. Part. Nucl. Phys. **101**, 177 (2018).
[31] A. Mengoni, The new n_TOF near station, CERN-INTC-2020-073/INTC-I-222 (2020), https://cds.cern.ch/record/2737308?ln=es.
[32] R. L. Macklin, J. Halperin, and R. R. Winters, Nucl. Instrum. Methods **164**, 213 (1979).
[33] C. Guerrero *et al.*, Nucl. Instrum. Methods Phys. Res. A **608**, 424 (2009).
[34] R. L. Macklin and J. H. Gibbons, Phys. Rev. **159**, 1007 (1967).
[35] U. Abbondanno *et al.*, Nucl. Instrum. Methods Phys. Res. A **521**, 454 (2004).
[36] C. Domingo-Pardo *et al.* (n_TOF Collaboration), Phys. Rev. C **74**, 055802 (2006).
[37] J. M. Belleman *et al.*, A new wall current monitor for the Cern proton synchrotron, in *Proceedings of the 5th International Beam Instrumentation Conference* (JACoW, Geneva, Switzerland, 2016).
[38] S. Marrone *et al.*, Nucl. Instrum. Methods Phys. Res. A **517**, 389 (2004).
[39] U. Abbondanno, Nucl. Instrum. Methods Phys. Res. A **538**, 692 (2005).
[40] A. Masi *et al.*, in *Proceedings of the 16th International Conference on Accelerator and Large Experimental Physics Control Systems* (JACoW, Geneva, Switzerland, 2018).
[41] E. Cano *et al.*, EPJ Web Conf. **245**, 04013 (2020).
[42] L. Mascetti *et al.*, J. Phys.: Conf. Ser. **664**, 042035 (2015).
[43] M. C. Moxon and E. R. Rae, Nucl. Instrum. Methods **24**, 445 (1963).

[44] J. Allison *et al.*, IEEE Trans. Nucl. Sci. **53**, 270 (2006).
[45] J. Allison *et al.*, Nucl. Instrum. Methods Phys. Res. A **835**, 186 (2016).
[46] Meng Wang, G. Audi, F. G. Kondev, W. J. Huang, S. Naimi, and X. Xinget, Chin. Phys. C **41**, 030003 (2017).
[47] E. Mendoza *et al.*, Nucl. Instrum. Methods Phys. Res. A **1047**, 167894 (2023).
[48] E. Mendoza, https://github.com/UIN-CIEMAT/NuDEX.
[49] S. Marrone *et al.* (The n_TOF Collaboration), Phys. Rev. C **73**, 034604 (2006).
[50] R. Terlizzi *et al.* (The n_TOF Collaboration), Phys. Rev. C **75**, 035807 (2007).
[51] N. M. Larson, *Updated User's Guide for Sammy: Multilevel R-Matrix Fits to Neutron Data Using Bayes' Equations*, Technical report (Oak Ridge National Laboratory (ORNL), Oak Ridge, TN, 2008).